Biosensors and Bioelectronics 134 (2019) 109–116

Contents lists available at ScienceDirect

Biosensors and Bioelectronics

journal homepage: www.elsevier.com/locate/bios

Dual-signal-amplified electrochemiluminescence biosensor for microRNA detection by coupling cyclic enzyme with CdTe QDs aggregate as luminophor

Hong-Yun Zhu, Shou-Nian Ding*

Jiangsu Province Hi-Tech Key Laboratory for Bio-medical Research, School of Chemistry and Chemical Engineering, Southeast University, Nanjing, 211189, China

ARTICLE INFO

Keywords:
Electrochemiluminescence (ECL) biosensor
$mSiO_2$@CdTe@SiO_2 (mSQS) NSs
Duplex-specific nuclease
Fe_3O_4@Au nanoparticles
MicroRNAs

ABSTRACT

In this work, a dual-signal-amplified electrochemiluminescence (ECL) biosensor was proposed for the first time to detect microRNAs (miRNAs) based on cyclic enzyme and seeded-watermelon-like mesoporous nanospheres ($mSiO_2$@CdTe@SiO_2, mSQS NSs). mSQS NSs were successfully fabricated by inlaying the CdTe quantum dots (QDs) into the mesoporous silica ($mSiO_2$) and future coating the surface with the silica layer. The obtained mSQS NSs contained tens of QDs and exhibited much stronger ECL signal than single QDs. The ECL biosensor achieved firstly signal amplification by using mSQS NSs to label the functional oligonucleotide probe (DNA-F) as enhanced ECL signal probes. Well-dispersed Fe_3O_4@Au nanoparticles were prepared as immobilization matrices to load hairpin-structured DNA probe (DNA-P). When the target miRNAs were present, hairpin DNA undertook conformation changes. Meanwhile, RNA/DNA duplexes was formed which cleaved by duplex-specific nuclease (DSN) to release miRNAs. Target miRNAs were cycled to hybridize with hairpin DNA, which achieved secondly signal amplification of the ECL biosensor. Thereafter, the complementarily parts between DNA-F and the rest DNA-P generated conjugates. The obtained conjugates would be collected on the surface of the electrode by effecting of magnet. Under the optimal conditions, the developed biosensor showed a wide linear range from 0.1 pM to 100 pM with a low detection limit of 33 fM (S/N = 3). The results of detection for the stability, specificity and reproducibility of ECL biosensor were outstanding. Simultaneously, the potential application of ECL biosensor was verified by using biosensor in serum sample.

1. Introduction

MicroRNAs (miRNAs), which were typically about 22 nucleotides long, single-stranded, endogenous and nonprotein coding RNAs, played vital roles as post-transcriptional regulators for gene expression and finally influenced a wide range of biological processes (Dong et al., 2013; Wahid et al., 2010). Recently, various intriguing studies demonstrated that the up or down expression of miRNAs had close relationship with the occurrence of various cancers (Ambs et al., 2008; Lu et al., 2005; Miller et al., 2016). Thus, miRNAs were proved as next-generation disease biomarkers for early diagnosis (Xue et al., 2014). However, the detection of miRNAs was a challenging task owing to short and highly homologous to each other. It was urgent demand to attach more attention to develop standing methods for miRNAs detection (Xiang, 2015). An excellent sensor would possess the following distinct advantages: (1) high sensitivity with low background interference (Ma et al., 2017); (2) simple operation process to save time and labor; (3) the low cost of the instrument (Xu et al., 2018). Up to now, many fascinating sensing methods were established for miRNAs detection. For example, electrochemical (Kong et al., 2016; Ren et al., 2017a; Su et al., 2017; Yang et al., 2014), fluorescence (FL) (Borghei et al., 2017; Liu et al., 2013; Miao et al., 2017b), colorimetric (Guo et al., 2017), electrochemiluminescence (ECL) (Feng et al., 2017; N et al., 2015; Ramji et al., 2014; Yang et al., 2017a). The analytical technique of ECL, which was equipped with many remarkable merits including high sensitivity, easy to operate and inexpensive instrument, received increasing attention (Debad et al., 2004; Guo et al., 2017; Xiao et al., 2017).

Since Bard et al. firstly reported the ECL of silica nanocrystals in 2002, variety of new luminescent reagents were applied to the ECL system (Ding et al., 2002). A new ECL luminophor called quantum dots (QDs) aroused extensive concern relying on its unique properties including controllable size, broad absorption, high photochemical stability and prominent biocompatibilities (Ding et al., 2002; Ren et al.,

* Corresponding author.
E-mail address: snding@seu.edu.cn (S.-N. Ding).

https://doi.org/10.1016/j.bios.2019.04.005
Received 6 March 2019; Accepted 1 April 2019
Available online 03 April 2019

2017b). In the family of QDs, cadmium-based QDs were widely used in biological sensing. Our groups reported several immunosensor which achieved high selectivity for different types biomarkers by using CdTe or CdZnTeS QDs as tags (Dong et al., 2017; Liang et al., 2018). To further increase the sensitivity, our groups reported a method of loading considerable illuminants based upon beads. Concretely, tens of CdTe QDs were incorporated into mesoporous silica nanoparticles ($mSiO_2$ NSs). However, the structure of mesoporous would result in not only cytotoxicity but also electrochemical instability because of leakage of cadmium (Hu et al., 2018). Therefore, evident advantages were identified by coating with nontoxic silica on $mSiO_2$@CdTe NSs (mSQ NSs). For instance, silica shell would effectively prevent the leak of QDs to increase the biocompatibility. In addition, the surface of silica shell was modified easily by functional groups such as carboxyl groups, amines and sulfhydryl groups, which resolved the limitations of binding to biomolecules (Zhu et al., 2012, 2013). The as-prepared nanomaterials with the structure like watermelon were named as seeded-watermelon-like mesoporous nanospheres ($mSiO_2$@CdTe@SiO_2, mSQS NSs).

In order to further improve the sensitivity of nucleic acid detection, some conventional strategies were used for miRNAs detection commonly, such as northern blotting, miRNA microarrays, quantitative reverse transcription PCR (qRT-PCR) and so on (Hao et al., 2015; Yang et al., 2014b). However, these methods had some problems, which required complex instruments or amplified the nonspecific background. Recently, the method based on nicking enzyme signal amplification (NESA) became a powerful tool in bioanalysis (Yin et al., 2012). Furthermore, duplex-specific nuclease (DSN) exhibited ultrahigh selectivity for miRNAs family members (Zhang et al., 2016). For this, DSN enzymes were able to distinguish short duplexes which were perfectly or imperfectly matched. As we all know, DSN enzymes could cleave DNA/RNA hybrid duplexes preferentially to hydrolyze DNA and release RNA but not for single-stranded DNA or miRNA sequence. Therefore, single miRNA sequence could bind to multiple hairpin probes, which was conducive to the obtained signal amplified immensely.

Nanoparticles (NPs) with unique function and outstanding biocompatibility have become excellent matrices in ECL immunosensor (Zhang et al., 2015a). Our previous works reported that Fe_3O_4 NPs were coated with silica shells or Au NPs as the matrices to immobilize primary antibodies (Liang et al., 2018; Zhang and Ding, 2017). In virtue of the unique optical property, catalytic activity and superparamagnetic property, Fe_3O_4@Au NPs served as an ideal platform for electrochemical assay to detect various analytes (Miao et al., 2017a; Wan et al., 2015; Zhang et al. 2015b, 2018). In this work, some requirements were satisfied for nanocarriers, for instance, high loaded site, good conductivity and low toxicity. Fe_3O_4@AuNPs became an ideal choice to serve as the desired nanocomposite (Yang et al., 2017b). Since hairpin-structured DNA probe (DNA-P) with a thiol group at one end would conjugated with Au NPs specifically through an easy process (Miao et al., 2017a).

Herein, an ultra-sensitive and easy to perform ECL biosensor was designed on account of functional oligonucleotide probe (DNA-F) labeled mSQS NSs and DNA-P hybridized Fe_3O_4@Au to detect miRNAs. The principle for biosensor with amplification ECL signal was illustrated in Scheme 1. Firstly, mSQS NSs were prepared as briefly outlined in Scheme 1 (A). Initially, $mSiO_2$ NSs were obtained by etching for SiO_2 NSs. Then, tens of QDs were incorporated into $mSiO_2$ NSs to synthesize mSQ NSs by the reaction of amino-functionalized $mSiO_2$ NSs with carboxylate-capped QDs. Subsequently, nontoxic silicon shell coated on the surface of mSQ NSs on the strength of Stöber method with slight modification to improve the biocompatibility (Ge and Yin, 2010; Z et al., 2015). The fabrication process of the ECL biosensor was shown in Scheme 1 (B). In this work, aminated mSQS NSs and DNA-F were cross-linked by glutaraldehyde as the signal unit of the sensor. Fe_3O_4@Au NPs with the convenience of magnetic separation and high surface area to volume ratio were employed as nanocarriers to immobilize DNA-P by Au-S bonding. Target miRNAs would hybridize with DNA-P to form conformation change and RNA/DNA duplexes. Then the duplexes were recognized and cleaved by DSN enzymes. MiRNAs released from duplexes were cycled to hybridize with hairpin DNA, which realized the recycling of target miRNAs. Meanwhile, the introducing of mSQS NSs was through the complementary pairing reaction of base between DNA-F with the rest DNA-P. After that, the biosensor was prepared and collected on the surface of the electrode by the action of a magnet. Enlightened by the above facts, the fabricated biosensor would be a powerful tool for miRNAs detection.

2. Experimental

2.1. Materials and reagents

6-Mercapto-1-hexanol (MCH) was supplied by Admas Reagent Co., Ltd. Tris (2-carboxyethyl) phosphine hydrochloride (TCEP) was purchased from J&K Scientific Ltd. (Beijing). Tris-HCl buffer solution (pH 7.4) was purchased from Biotopped Life Sciences Co., Ltd. DSN and 10 × DSN master buffer (500 mM Tris-HCl, 50 mM $MgCl_2$, 10 mM DTT, pH 8.0) were purchased from Evrogen (Moscow, Russia). HPLC-purified, synthetic miRNAs and all other oligonucleotides were purchased from Sangon Biological Engineering Technology and Services Co., Ltd. (Shanghai, China), and their sequences were shown in Supporting Information. All other reagents were displayed in Supporting Information, which were analytical grade.

2.2. Apparatus

A conventional three-electrode system composed of glassy carbon working electrode (GCE, diameter 3 mm) as working electrode, platinum (Pt) wire as counter electrode, a saturated calomel electrode (SCE) as reference electrode was applied in this work. Electrochemical experiments were performed with a CHI 660E electrochemical workstation (CHI, China). The ECL intensity measurements were carried out with MPI-E multifunctional electrochemical and chemiluminescent analytical system (Xi'an Remex Analytical Instrument Co., Ltd.). The estimation of the amount of surface-modified DNA was completed in NanoDrop 2000. And other instruments were shown in the Supporting Information.

2.3. Bioconjugation of mSQS-/DNA-P

The synthetic methods of CdTe QDs and mSQ were described in the Supporting Information. The synthesis and amination procedures of mSQS NSs were considerably modified according to previous reported in the literature (Ge and Yin, 2008; Li et al., 2015). In brief, 50 mg of mSQ NSs was dispersed in a mixture of ethanol and water, and the solution stirred for 30 min vigorously. Then, the pH value of the solution was adjusted to 9 by adding ammonia gradually. Next, TEOS (0.2 mL) was injected into the solution, and the solution was kept stirred for 10 h. The products of mSQS NSs were obtained by precipitating and washing with centrifugation. Subsequently, the products were dissolved in a mixture of ethanol and water. Similarly, aqueous ammonia was used to adjust the pH to 9. Then the solution was stirred vigorously at room temperature (RT) for 8 h after injected TEOS and APTES. The aminated mSQS NSs were washed and stored at 4 °C for further use.

Glutaraldehyde (GA) was utilized to assemble aminated mSQS NSs and DNA-F through cross-linking reaction. 10 mg of aminated mSQS NSs was dissolved in 7.5 mL of ultrapure water, and then 2.5 mL of GA solution (2.5 wt%) was added to the above solution and the solution was stirred vigorously at RT for 6 h. The mixture was washed several times with 10 mM PBS (pH 7.4) to remove excess GA. 0.5 mL of DNA-F (2 μM) was mixed with 0.5 mL mSQS NSs (5 mg/mL) in PBS (10 mM, pH 7.4). The mixture was allowed to react for 5 h under soft shaking at RT. The products were purified several times and dispersed in 1 mL of PBS

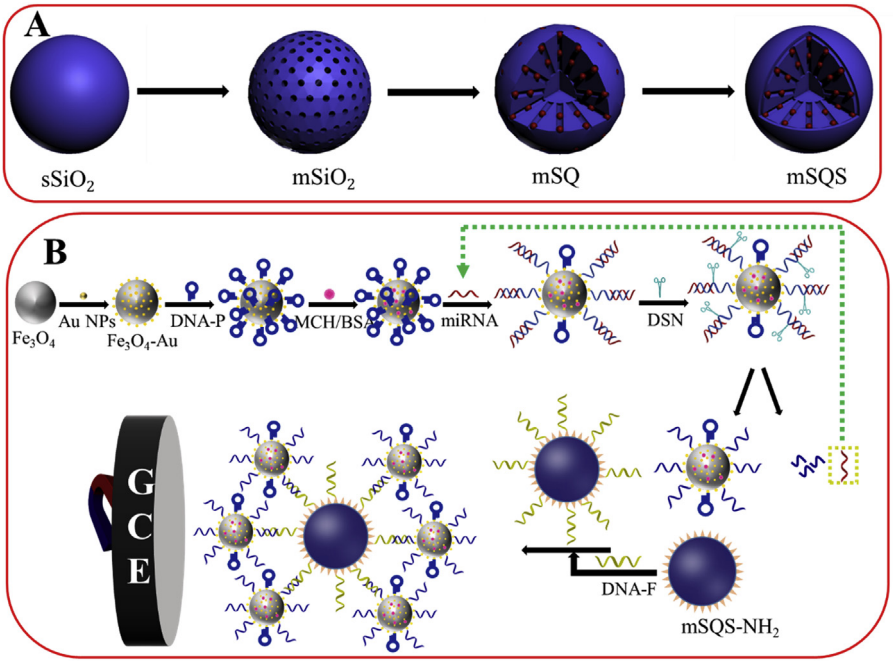

Scheme 1. Synthesis process of seeded-watermelon-like mesoporous nanospheres (A); schematic illustrations of fabrication process of proposed ECL biosensor (B).

(10 mM, pH 7.4). Finally, the mSQS/DNA-F was incubated in PBS solution containing BSA (200 μL, 1.0 wt%) to block the nonspecific binding sites. After washed, the products were dissolved in 1 mL PBS and stored at 4 °C for future use.

2.4. Preparation of Fe_3O_4@Au/DNA-P

The process of preparation of the Fe_3O_4@Au NPs was presented in the Supporting Information. The conjugation between Fe_3O_4@Au NPs and DNA probe was carried out via similar procedures in previous reports with slight changes (Lu et al., 2016; Miller et al., 2016; Zhang et al., 2016a). Pristine Fe_3O_4@Au NPs were dissolved in double-distilled water with the concentration of 2 mg/mL. DNA-P probe was prepared in the buffer solution (10 mM Tris-HCl, 1 mM EDTA, 10 mM TCEP, and 0.1 M NaCl). Next, DNA probe was blended the Fe_3O_4@Au NPs colloid for all night with the final concentration of 1 μM. After that, the Fe_3O_4@Au/DNA-P conjugates were incubated in 0.1 mM MCH for 0.5 h and 1% BSA solution for1 h respectively to block the nonspecific active binding sites. Finally, the conjugates were washed and redispersed in PBS solution as above, and reserved at 4 °C for future applications.

2.5. Fabrication of the ECL biosensor

The fabrication process of the magnetic biosensor was described as Scheme 1. At first, various concentrations of miRNA-182 and 0.1 U DSN enzyme were injected into the Fe_3O_4@Au/DNA-P solution respectively, and then the solution was shaken gently at 37 °C for 40 min. Afterwards, the 1 × DSN stop solution was added into mixture solution for 5 min. Next, mSQS/DNA-F was added into above solution for 3 h. After magnetic cleaned, biosensor was redispersed in PBS and stored at 4 °C.

2.6. ECL measurement

In a typical ECL assay, 6 μL of the biosensor with different concentrations of miRNAs was dropped on the pretreated GCE which dried at RT. The ECL tests were conducted in 0.1 M PBS solution (pH 7.4) containing 0.05 M TPrA. And the ECL measurements were performed from 0 to 1.3 V at the scan rate of 100 mV/s. Pt wire and saturated SCE electrode were used as the counter electrode and reference electrode, respectively. The photomultiplier tube (PMT) voltage was set at 900 V.

3. Results and discussion

3.1. Characterization of the mSQS NSs

The morphologies of CdTe QDs were characterized by transmission electron microscopy (TEM) in Fig. S-1A. The inset was high-magnification transmission electron microscopy (HRTEM) of CdTe QDs. An average diameter of the round QDs was 3.2 nm, which demonstrated distribution was relatively uniform. Fig. 1 displayed a typical TEM image and particle size distributions of solid SiO_2 ($sSiO_2$) NSs, $mSiO_2$ NSs, mSQ NSs and mSQS NSs relatively. It can be observed that the prepared $sSiO_2$ NSs possessed uniform size and well-dispersion with an average diameter of 585 nm (Fig. 1A–C). Compared with $sSiO_2$ NSs, the average particle diameter of $mSiO_2$ NPs decreased to 525 nm by the reaction of surface etch (Fig. 1D–F). As shown in Fig. 1G–I, large amounts of QDs were attached to $mSiO_2$ NSs through covalent interaction, and it can be seen that monodispersed nanoparticles with an average diameter of 548 nm were well dispersed. After wrapped silicon shell outside the mSQ NSs through Stöber's process, the average particle size of mSQS NSs increased to 577 nm (Fig. 1J-L). The magnification TEM image displayed the thickness of the silicon shell was 11 nm (inset Fig. 1K).

The measurement of nitrogen adsorption/desorption isotherms was carried out to indicate the effect of etch by NaOH and loaded capacity of mesoporous nanospheres (Fig. S-2A). The $sSiO_2$ prepared by stöber method owned the property of nonporous. The obvious hysteresis loop of cure b demonstrated mesopores were generated in $mSiO_2$ NSs, and the mean pore size was 9.3 nm (Fig. S-2B). As describe in Fig. S-1, the average diameter of the round QDs was 3.2 nm, which was smaller than the pore. The BET surface area reduced from 170 m^2/g to 146 m^2/g after the QDs were embedded in the mesopores. Ulteriorly, the silicon layer outside the mSQ closed the pores on the surface, resulting in a further decrease to 140 m^2/g of the amount of adsorption.

To verify that mass of CdTe QDs were embedded into seeded watermelon-like mesoporous nanospheres mSQS NSs, confocal fluorescence images were also performed. In the test, nanoparticles produced

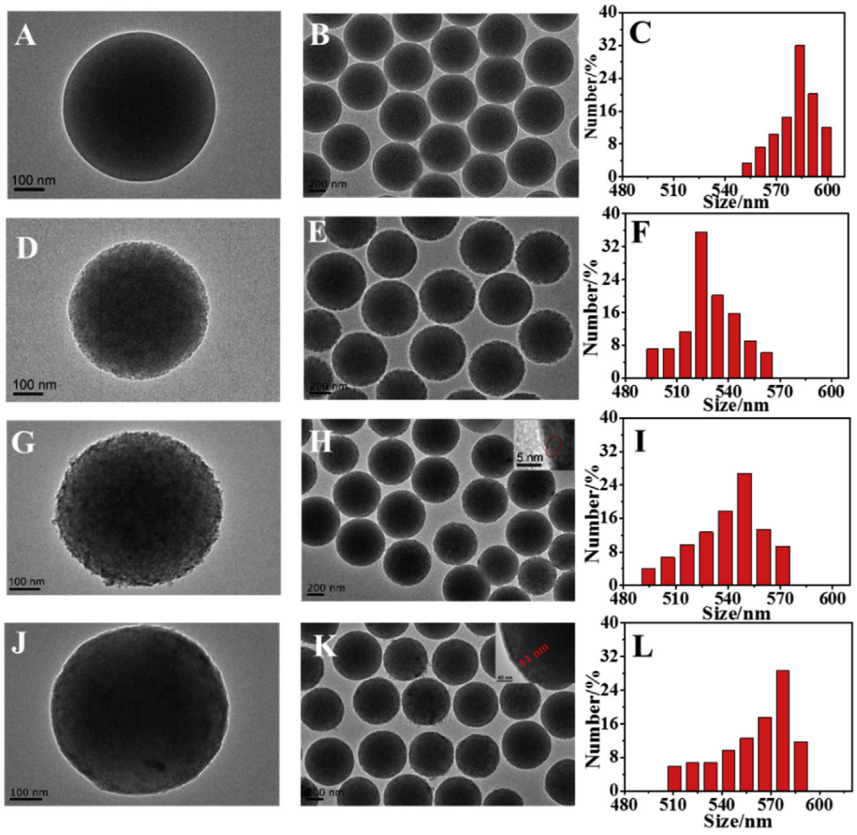

Fig. 1. TEM images of $sSiO_2$ NSs (A, B), $mSiO_2$ NSs (D, E), mSQ NSs (G,H), and mSQS NSs (J,K) and particle size distributions of $sSiO_2$ NSs (C), $mSiO_2$ NSs (F), mSQ NSs (I) and mSQS NSs (L). HR-TEM image of mSQ NSs (inset H) and the thickness of silicon shell (inset K). (For interpretation of the references to color in this figure legend, the reader is referred to the Web version of this article.)

red fluorescence under green light excitation. The excellent dispersibility of nanospheres was proved in Fig. S-3A-C, and the QDs were uniformly embedded in the surface and inside of mesoporous silica nanoparticles.

Optical properties of seeded mSQS NSs were studied and displayed in Fig. 2. The UV-vis absorption spectrum of CdTe QDs, mSQ NSs and mSQS NSs showed an excitonic peak at 635 nm, 674 nm and 658 nm, severally (Fig. 2A). Fig. 2B displayed the PL spectra of the CdTe QDs, mSQ NSs and mSQS NSs, and revealed the 39 nm red-shift of absorbance peak compared to CdTe QDs, probably because of the sharp change in the zeta potential of the solution. In contrast with mSQ NSs, a slight blue-shift in the fluorescence peak of mSQS NSs was observed, owing to the etching of CdTe QDs caused by ammonia probably. The corresponding fluorescence photographs under 365 nm light excitation were exhibited in the inset of Fig. 2B.

As described in Fig. 3A, a very low ECL emission of bare GCE (curve a) was observed, which indicated the background signal had a negligible influence for the detection. The ECL intensity of mSQ NSs (curve c) was higher than that of QDs (curve b) because the $mSiO_2$ NPs was inlaid with a large number of QDs. After wrapped a layer of silicon shell, the ECL intensity of mSQS NSs (curve d) declined because the silicon shell hindered the transmission of some electrons. Inset was corresponding cyclic voltammetry (CV) curves. The reason of significant increase in the mSQ NSs current signal is that large numbers of QDs were incorporated into the $mSiO_2$ NPs with the porous structure (curve c). On the contrary, the current of mSQS NSs (curve d) reduced because the outer cladding of the silicon shell hindered the mass diffusion and reduced the specific surface area. In Fig. 4B, the ECL spectrum revealed a main peak at 682 nm, which was very close to the FL spectrum. And it indicated that the surface had been largely passivated.

3.2. Characterization of Fe_3O_4@Au NPs

As shown in Fig. S-4, scanning electron microscopy (SEM) was

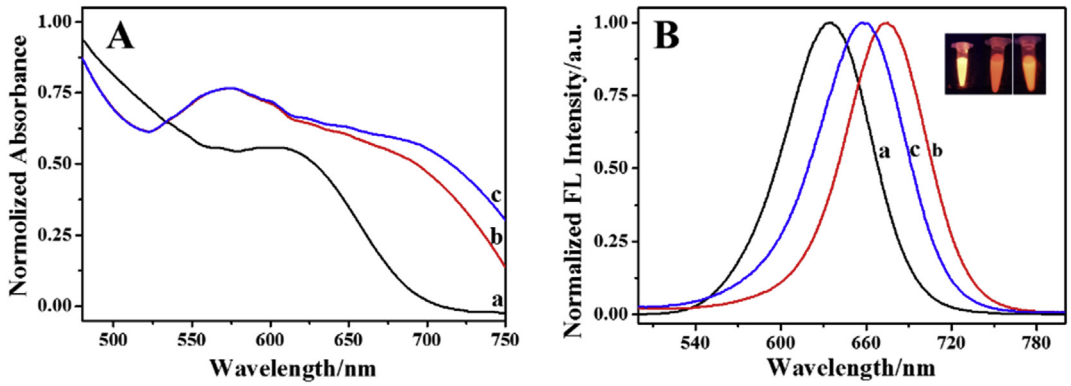

Fig. 2. The UV-vis (A) and FL (B) spectra of CdTe QDs (a), mSQ NSs (b) and mSQS NSs (c); Inset: Photographs of CdTe QDs, mSQ NSs and mSQS NSs under 365 nm UV lamp.

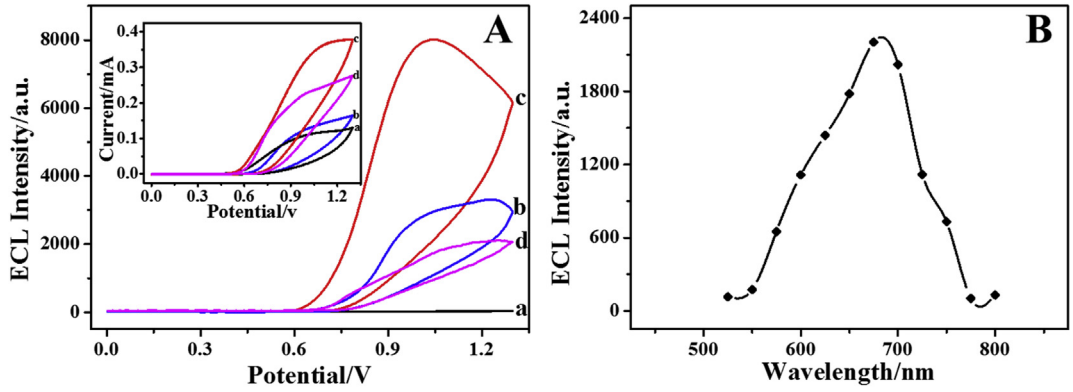

Fig. 3. ECL performance (A) of bare GCE (a), CdTe QDs (b), mSQ NSs (c) with PMT was set at 400 V and mSQS NSs (d) with PMT was set at 500 V; Inset was corresponding CV curves; The ECL spectrum (B) of mSQS NSs modified on GCE under filter (525 nm-800 nm).

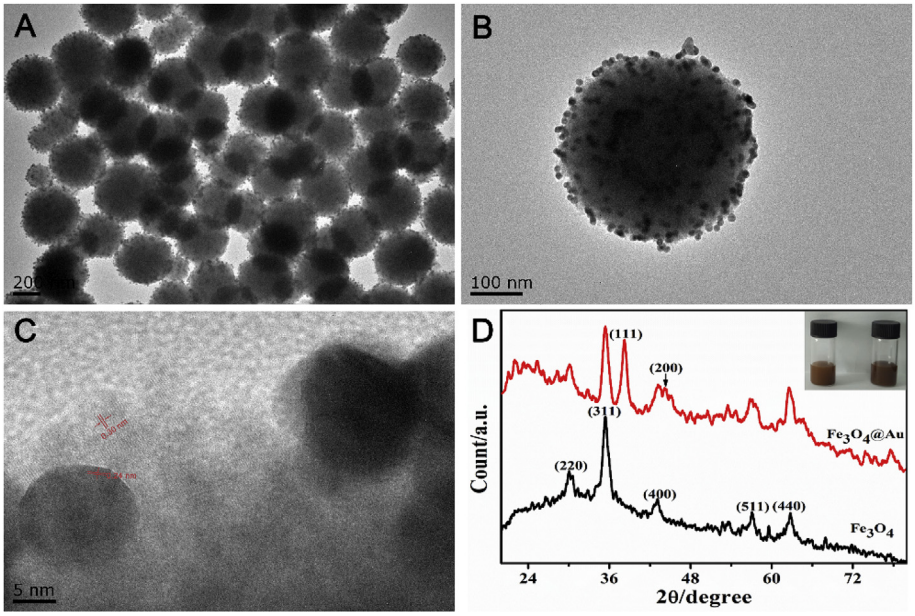

Fig. 4. TEM images of Fe_3O_4@Au NPs (A) and the magnification (B); HRTEM of Fe_3O_4@Au NPs (C); XRD patterns of Fe_3O_4 NPs and Fe_3O_4@Au NPs (Inset: photographs of correspondent nanocomposites) (D).

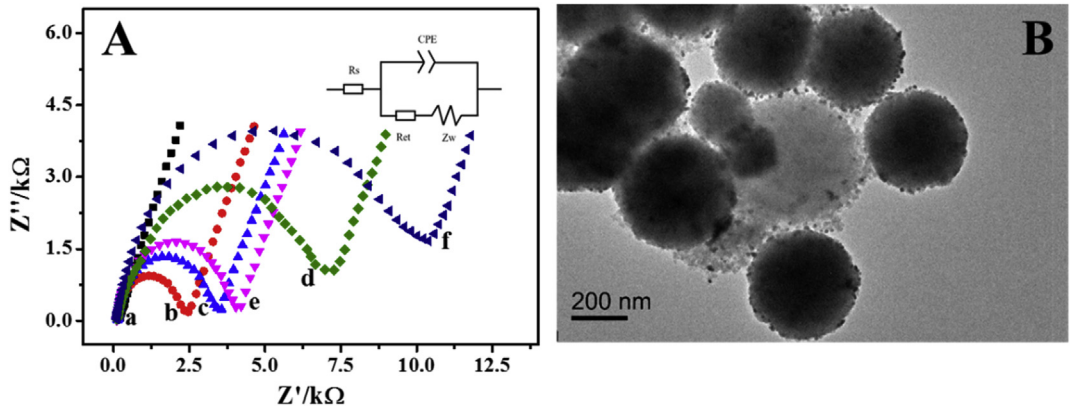

Fig. 5. EIS responses (A) of different modified electrodes: (a) bare GCE; (b) Fe_3O_4-Au/DNA-P/GCE; (c) MCH/Fe_3O_4-Au/DNA-P/GCE; (d) BSA/MCH/Fe_3O_4-Au/DNA-P/GCE; (e) miRNAs/BSA/MCH/Fe_3O_4-Au/DNA-P/GCE; (f) the structure of biosensor formed by hybridization with mSQS/DNA-F. Inset: the equivalent circuit applied to fit the impedance data. TEM image (B) of ECL biosensor.

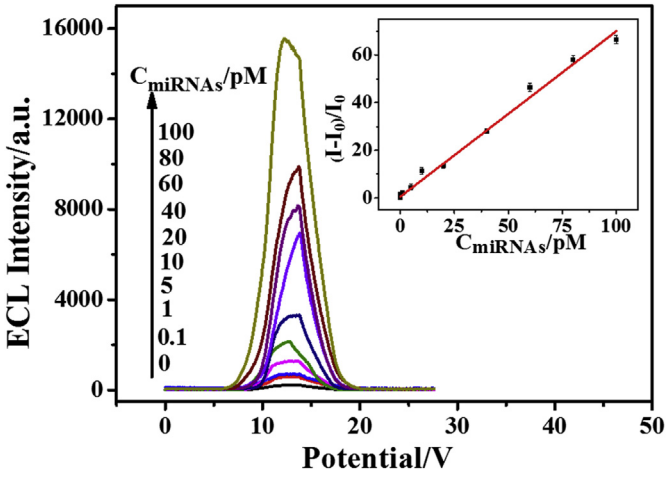

Fig. 6. ECL intensity of the sensor in the presence of different concentration of miRNAs (pM). All the ECL signals were measured in PBS (0.1 M, pH 7.4) containing 50 mM TPrA. The voltage of the PMT was set at 900 V. Inset: Calibration curve for miRNAs determination.

employed to characterize the morphologies and structures of Fe_3O_4 NPs and Fe_3O_4@Au NPs. Fig. S-4A revealed that Fe_3O_4 NPs were spherical with rough surfaces, and the average size was about 360 nm. Fig. S-4B showed the SEM images of Fe_3O_4@Au NPs, which indicated that large amounts of Au NPs were decorated on the Fe_3O_4 NPs homogeneously and densely.

The morphologies and structures of Fe_3O_4@Au NPs were also characterized by TEM. The typical TEM image of Fig. 4A showed the excellent dispersion of Fe_3O_4@Au NPs, and the high-density Au NPs could be clearly observed in the surface of Fe_3O_4 NPs. The amplified TEM image (Fig. 4B) revealed that the diameters of Au NPs were 13 ± 2 nm. A HRTEM image of the Fe_3O_4@Au NPs (Fig. 4C) indicated that a series of 2D lattice fringes were examined to be 0.30 nm and 0.24 nm, respectively, which was similar to the lattice spacing (220) plane of the centered cubic structure of magnetite and the (111) plane of the centered cubic structure of Au (Wei et al., 2015). The composition and crystallinity of the as-prepared Fe_3O_4 NPs and Fe_3O_4@Au NPs were further characterized by X-ray diffraction (XRD) (Fig. 4D). The XRD pattern of Fe_3O_4 NPs sample exhibited seven diffraction peaks (30.00°, 35.32°, 43.12°, 53.47°, 56.90°, 62.43° and 74.34°), which corresponded to the (220), (311), (400), (422), (511), (440) and (442) planes of inverse spinel structured magnetite (JCPDS card no. 19-0629) (Gao et al., 2014; Lin and Doong, 2011; Wang et al., 2013). After coated with Au NPs, four new peaks at 38.4°, 44.6°, 64.9°, and 77.8° were observed, which consistent with the (111), (200), (220) and (311) planes of the face centered cubic structured gold (JCPDS card no. 04-0784) (Sun and Xia, 2003). As shown, an increase in the reflection intensity of Au was attributed to the linkage of Au to the Fe_3O_4 NPs probably. The above results further testified the successful construction of Fe_3O_4@Au NPs.

Magnetic measurements of the as-prepared Fe_3O_4 NPs, aminated Fe_3O_4 NPs and Fe_3O_4@Au NPs were measured using a vibrating sample magnetometer (VSM) at 294 K. Magnetization curves in Fig. S-5 displayed that the saturation magnetization (Ms) values of Fe_3O_4 and Fe_3O_4@Au was about 60 emu/g and 52 emu/g at 15 kOe, severally, and the difference of Ms between Fe_3O_4 NPs and aminated Fe_3O_4 NPs was not apparent. The strong magnetic of Fe_3O_4@Au were sufficient to be separated rapidly (less than 1 min) under the external magnetic field.

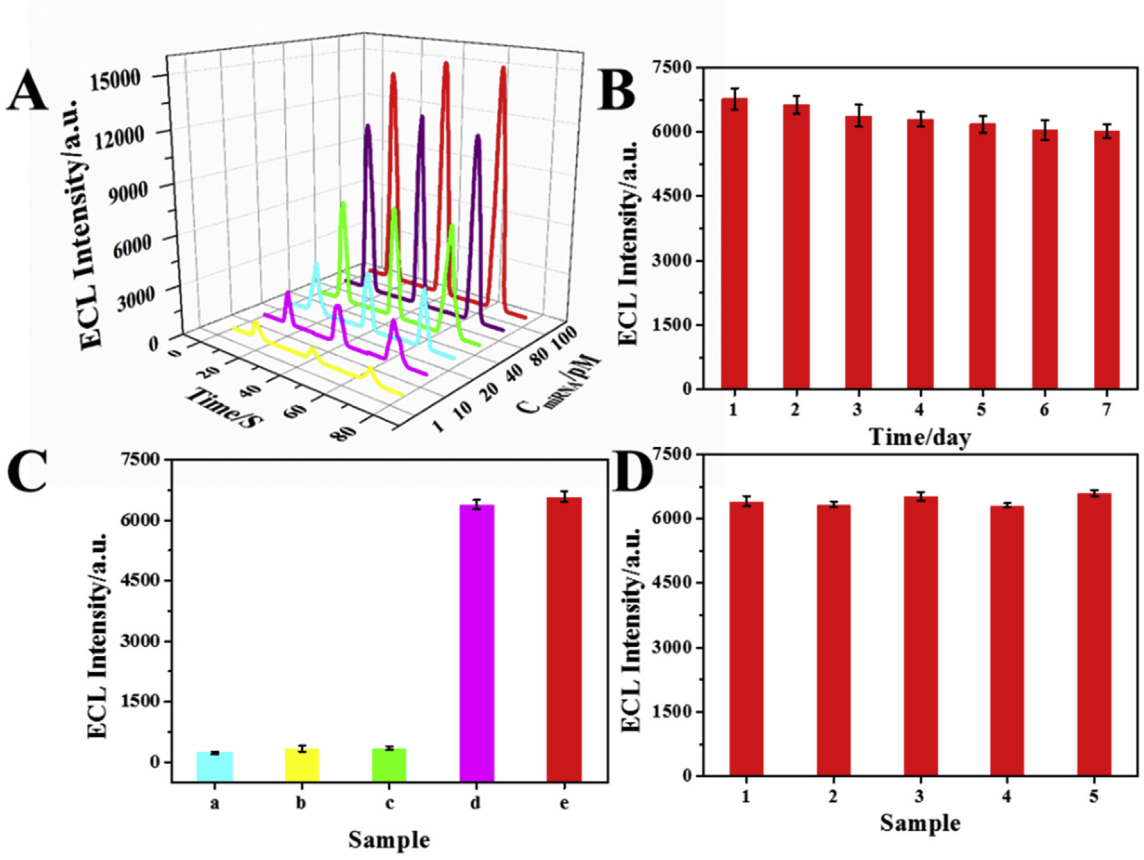

Fig. 7. ECL signals under continuous scan at different concentration of miRNA-182(A); Storage stability of the ECL biosensor(B); Specificity of the obtained biosensor (C) when analyzed with blank (a), miRNA-183 (100 pM) (b), miRNA-96 (100 pM) (c), miRNA-183 (100 pM) + miRNA-96 (100 pM) + miRNA-182 (40 pM) (d) and miRNA-182 (40 pM) (e). Reproducibility studies of the ECL biosensor (D). Error bar = RSD (n = 3).

The decrease in Ms was mainly due to the loading of the high density of Au NPs, which produced diamagnetic contribution. In the inset, the coercivity (Hc) and remanences (Mr) can be found, 9.8 Oe and 1.1 emu/g for Fe_3O_4@Au, 9.5 Oe and 0.8 emu/g for Fe_3O_4@Au. The slight Hc and Mr showed typical properties of superparamagnetic. Consequently, the Fe_3O_4@Au NPs attracted to the wall of the vial can be redispersed after taking away the magnet.

3.3. Characterization of Fe_3O_4@Au/DNA-P

The construction of Fe_3O_4@Au/DNA-P was characterized by UV-vis spectra. In Fig. S-6, a distinct peak at 560 nm was characterized (curve a) by examining Au NPs solution, which was correlated to the surface plasmon resonance (SPR) (Mezni et al., 2013; Zhou et al., 2010). Pure DNA solution showed a characteristic absorbance peak at 260 nm (curve b). Fe_3O_4 NPs presented no evaluable features in UV-vis region (curve c). After Au NPs were dropped on the Fe_3O_4 NPs surface, a broad absorption peak at 560 nm was observed, which was ascribed to the typical surface plasmon resonance (SPR) peak of Au (curve d) (Lei et al., 2012; Wang et al., 2010). In addition, two distinct peaks located at 260 and 530 nm could appeared after DNA-P conjugated with Fe_3O_4@Au NPs, which indicated the successful attachment of DNA onto Fe_3O_4@Au NPs (curve e).

3.4. Characterization of mSQS/DNA-F

The subtraction method was applied to estimate the amount of DNA modified the mSQS NPs surface by NanoDrop. Mean value was adopted under multiple measurements to ensure the accuracy. The concentrations of before or after incubating with mSQS NPs of DNA-F were 11.9 ng/μL and 2.8 ng/μL, which illustrated the concentration of DNA-F combined with mSQS NPs was 9.1 ng/μL (Tables S–2).

3.5. Optimization of experimental conditions

In order to improve the accuracy and sensitivity of the experiment, condition optimization was conducted. The DSN enzyme, which was vigorous under the appropriate temperature of 37 °C, pH value of 7.4 and presence of 5 mM Mg^{2+}, was used in present work. Admittedly, the incubation time and amount of DSN enzymes were studied by using the miRNA-182 target to ensure the amplification authority. As illustrated in Fig. S-7A, the ECL intensity increased immediately with the increase of DSN enzyme from 0.02 U to 0.10 U, and its intensity changed feeble subsequently. Thus, 0.1 U DSN enzymes were considered to the optimal amount used throughout subsequent experiments. As displayed in Fig. S-7B, increased incubation time for 0 min till 40 min caused the enhancement of ECL intensity and reached a plateau at 40 min. Therefore, 40 min incubation was sufficient for the further detection. Additionally, the concentration and incubation time of DNA-P were investigated. The inset in Fig. S-7C and D showed that the ECL signal increased with the increase of DNA-P concentration and incubation time, and reached the maximum at 1 μM and 12 h, respectively.

3.6. Characterizations of immunosensor fabrication

Electrochemical Impedance Spectroscopy (EIS) was employed to investigate the interface properties of the modified electrodes. Each fabrication process of the proposed biosensor was characterized by EIS in a solution of 0.1 M KCl containing 5 mM $[Fe(CN)_6]^{2-}/[Fe(CN)_6]^{3-}$. The semicircle diameter measured by the EIS indicated the electron transfer resistance (R_{et}), which directly controlled the electron transfer kinetics of the redox probe at the electrode interface. As shown in Fig. 5A, a small semicircle domain indicated that a bare GCE was obtained for the construction of a biosensor (curve a). The electrode modified with Fe_3O_4@Au/DNA-P led to increasing (R_{et} = 244.4 Ω, curve b). Then, incubation in MCH to block residual active site caused an increase in R_{et}, which could hinder charge transfer between the electroactive probe and the electrode surface (curve c). Then an increase of R_{et} was observed through incubating by BSA, which could be attributed to the insulating property of protein molecules (curve d). After DNA-P modified Fe_3O_4@Au NPs hybridized with miRNAs, R_{et} decreased (curve e). The reason was that the hybridization-induced opening of the magnetic probe with the immobilized hairpin structure, which made the $[Fe(CN)_6]^{3-/4-}$ molecule more accessible to the electrode surface. Next, incubation of mSQS NSs with DNA-F lead to R_{et} increasing significantly (curve f). The result of EIS confirmed the biosensor was fabricated successfully. It was worthwhile to notice that stability plays a vital role in biosensor. The inset in Fig. 5A was the equivalent circuit applied to fit the impedance data. Rs was solution resistance; CPE was constant phase angle element; Ret was electron-transfer resistance and Zw was Warburg diffusion resistance.

As illustrated in Fig. 5B, the morphology of ECL biosensor was investigated by TEM. Through the complementary pairing between the bases, several Fe_3O_4@Au/DNA-P were scattered around mSQS/DNA-F. It can be seen that the image was consistent with schematic illustration of fabrication process of ECL biosensor, which further demonstrated that the ECL biosensor was successfully constructed.

3.7. Quantitative detection of miRNA-182

MiRNA-182 was detected by the proposed biosensor. The increase of target concentration contributed to more conformational change of DNA-P, which was beneficial to the attachment of DNA-F labeled mSQS NSs. Therefore, ECL intensity enhanced with the increasing miRNAs concentration, and the result was described in Fig. 6. A linear response was observed from 0.1 to 100 pM. The linear regression equation was expressed as $I = 0.694\ c + 0.58$ (c, fM) with the correlation coefficient of 0.995. The detection limit was estimated to be 33 fM according to the S/N of 3. I represented the ECL intensity. The comparison for linear range and the detection limit between existing miRNAs detection biosensors and proposed biosensor in this work was listed in Tables S–3. The results suggested that the proposed approach was superior to that of most methods developed for miRNA-182 detection.

3.8. Evaluation of stability, specificity and reproducibility for ECL biosensor

The ECL stability was investigated adequately through testing the ECL signal with different concentrations repeatedly and testing the ECL signal periodically. As can be seen from Fig. 7A, ECL intensity was relatively stable under continuous scan at different concentrations of miRNAs. Moreover, the ECL intensity retained 88.7% of its initial value after stored at 4 °C for a week (Fig. 7B). The experimental result indicated that the stability of the using system was superior.

The specificity of the ECL biosensor was another crucial parameter. MiRNA-183 and miRNA-96 as interferences, which possessed 4-bases and 11-bases mismatched relative to miRNA-182, were determined. As demonstrated in Fig. 7C, the ECL intensity was almost the same with the blank sample when the interfering agents were incubated alone. Conversely, the ECL intensity exhibited conspicuous signals when the interferences coexisted with miRNA-182 or miRNA-182 existing alone. It is worth noticing that no significant difference of ECL signal was observed between cylinder d and e. The results demonstrated the satisfactory specificity of the designed biosensor.

Reproducibility was monitored in Fig. 7D to confirm its vital roles in sensing systems. Five batches of ECL biosensors were prepared in parallel with the same concentration of miRNAs (40 pM). In order to reduce the absolute deviation caused by the difference between the electrodes, the ECL intensity was detected on the same electrode. The RSD of measurements was about 2.86%, which demonstrated that the ECL biosensor endows excellent reproducibility.

3.9. Real sample analysis

The ECL biosensors was applied in human serum sample obtained from Nanjing Zhongda Hospital to confirm the accuracy of the proposed sensor for real sample assays in clinic system. The results of multiple serum samples assayed with our method were exhibited in Tables S–4, which was in good agreement with the concentration provided by hospital. The abovementioned results indicated that the proposed biosensor accurately measured the CEA concentration in the real sample.

4. Conclusions

In conclusion, a promising ECL biosensor was developed for miRNAs detection based on mSQS/DNA-F and Fe_3O_4@Au/DNA-P. Seeded-watermelon-like mSQS NSs inlaid vast QDs couple with DSN enzyme amplified ECL signal in this detection system. Through a series of verification, the established method demonstrated satisfactory sensitivity, excellent stability, pleasing selectivity and good accuracy, which was potentially applicable to detect wide cancer biomarkers in clinic diagnostics.

Declaration of interests

The authors declare that they have no known competing financial interests or personal relationships that could have appeared to influence the work reported in this paper.

Acknowledgments

This work was supported by the National Key Research and Development Program of China (2017YFA0700404), the National Natural Science Foundation of China (21535003, 21575022), the Key Research & Development Plan of Jiangsu Province (BE2018617),the Fundamental Research Funds for the Central Universities (2242016K41055), Qing Lan Project, A Project Funded by the Priority Academic Program Development of Jiangsu Higher Education Institutions (1107047002).

Appendix A. Supplementary data

Supplementary data to this article can be found online at https://doi.org/10.1016/j.bios.2019.04.005.

References

Ambs, S., Prueitt, R.L., Yi, M., Hudson, R.S., Howe, T.M., Petrocca, F., Wallace, T.A., Liu, C.G., Volinia, S., Calin, G.A., 2008. Cancer Res. 68 (15), 6162–6170.
Borghei, Y.S., Hosseini, M., Ganjali, M.R., 2017. Microchim. Acta 184 (8), 2671–2677.
Debad, J.D., Bard, A.J., Wightman, R.M., Buda, M., Choi, J.P., Danielson, N.D., Forry, S.P., Glezer, E.N., Maloy, J.T., Leland, J.K., 2004. Electrogenerated Chemiluminescence. Marcel Dekker.
Ding, Z.F., Quinn, B.M., Haram, S.K., Pell, L.E., Korgel, B.A., Bard, A.J., 2002. Science 296 (5571), 1293–1297.
Dong, H., Han, T.T., Ren, L.L., Ding, S.N., 2017. J. Electroanal. Chem. 806, 32–40.
Dong, H., Lei, J., Ding, L., Wen, Y., Ju, H., Zhang, X., 2013. Chem. Rev. 113 (8), 6207–6233.
Feng, Q.M., Shen, Y.Z., Li, M.X., Zhang, Z.L., Zhao, W., Xu, J.J., Chen, H.Y., 2017. Anal. Chem. 88 (1), 937–944.
Gao, Q., Zhao, A., Guo, H., Chen, X., Gan, Z., Tao, W., Zhang, M., Wu, R., Li, Z., 2014. Dalton Trans. 43 (21), 7998–8006.
Ge, J., Yin, Y., 2010. Adv. Mater. 20 (18), 3485–3491.
Ge, J.P., Yin, Y.D., 2008. Adv. Mater. 20 (18), 3485–+.
Guo, Q., Bian, F., Liu, Y., Qu, X., Hu, X., Sun, Q., 2017. Chem. Commun. 53 (36), 4954–4957.
Hao, N., Dai, P.P., Yu, T., Xu, J.J., Chen, H.Y., 2015. Chem. Commun. 51 (70), 13504–13507.
Hu, Y., Miao, Z.Y., Zhang, M.J., Yang, X.T., Tang, Y.Y., Yu, S., Shan, C.X., Wen, H.M., Zhu, D., 2018. Anal. Chem. 90 (9), 5678–5686.
Kong, D., Bi, S., Wang, Z., Xia, J., Zhang, F., 2016. Anal. Chem. 88 (21), 10667–10674.
Lei, L., Yu, K., Zhang, Z., Huang, R., Wang, Y., Zhu, Z., 2012. Appl. Surf. Sci. 258 (22), 8521–8526.
Li, Z., Wang, Y., Ni, Y.N., Kokot, S., 2015. Biosens. Bioelectron. 70, 246–253.
Liang, X.L., Bao, N., Luo, X., Ding, S.N., 2018. Biosens. Bioelectron. 117, 145–152.
Lin, F., Doong, R., 2011. J. Phys. Chem. C 115 (14), 6591–6598.
Liu, H., Xu, S., He, Z., Deng, A., Zhu, J.J., 2013. Anal. Chem. 85 (6), 3385–3392.
Lu, J., Getz, G., Miska, E.A., Alvarezsaavedra, E., Lamb, J., Peck, D., Sweetcordero, A., Ebert, B.L., Mak, R.H., Ferrando, A.A., 2005. Nature 435 (7043), 834–838.
Lu, Z., Tang, H., Wu, D., Xia, Y., Wu, M., Yi, X., Li, H., Wang, J., 2016. Biosens. Bioelectron. 86, 502–507.
Ma, H., Zhao, Y., Liu, Y., Zhang, Y., Wu, D., Li, H., Wei, Q., 2017. Anal. Chem. 89 (24), 13049–13053.
Mezni, A., Balti, I., Mlayah, A., Jouini, N., Smiri, L.S., 2013. J. Phys. Chem. C 117 (31), 16166–16174.
Miao, P., Tang, Y., Wang, L., 2017a. ACS Appl. Mater. Interfaces 9 (4), 3940–3947.
Miao, X., Cheng, Z., Ma, H., Li, Z., Xue, N., Wang, P., 2017b. Anal. Chem. 90 (2), 1098–1103.
Miller, K.D., Siegel, R.L., Lin, C.C., Mariotto, A.B., Kramer, J.L., Rowland, J.H., Stein, K.D., Alteri, R., Jemal, A., 2016. Ca-Cancer J. Clin. 66 (4), 271–289.
N, H., PP, D., T, Y., JJ, X., HY, C., 2015. Chem. Commun. 51 (70), 13504–13507.
Ramji, R., Wang, M., Bhagat, A.A.S., Weng, D.T.S., Thakor, N.V., Lim, C.T., Chen, C.H., 2014. Biomicrofluidics 8 (3), 47–53.
Ren, X., Zhang, T., Wu, D., Yan, T., Pang, X., Du, B., Lou, W., Wei, Q., 2017a. Biosens. Bioelectron. 94, 694–700.
Ren, L.L., Dong, H., Han, T.T., Chen, Y., Ding, S.N., 2017b. Analyst 142 (20), 3934–3941.
Su, S., Cao, W., Liu, W., Lu, Z., Zhu, D., Chao, J., Weng, L., Wang, L., Fan, C., Wang, L., 2017. Biosens. Bioelectron. 94, 552–559.
Sun, Y., Xia, Y., 2003. Analyst 128 (6), 686–691.
Wahid, F., Shehzad, A., Khan, T., Kim, Y.Y., 2010. Biochim. Biophys. Acta 1803 (11), 1231–1243.
Wan, Q., Chen, S., Shi, W., Li, L., Ma, H., 2015. Angew. Chem. 126 (41), 11096–11100.
Wang, X., Lou, X., Wang, Y., Guo, Q., Fang, Z., Zhong, X., Mao, H., Jin, Q., Wu, L., Zhao, H., 2010. Biosens. Bioelectron. 25 (8), 1934–1940.
Wang, Z., Wu, L., Wang, F., Jiang, Z., Shen, B., 2013. J. Mater. Chem. 1 (34), 9746–9751.
Wei, J., Li, S.S., Zheng, G., Xing, C., Liu, J.H., Huang, X.J., 2015. Anal. Chem. 88 (2), 1154–1161.
Xiang, Y., 2015. ACS Appl. Mater. Interfaces 7 (2), 1188–1193.
Xiao, T., Zhang, B., Zou, G., 2017. J. Am. Chem. Soc. 139 (25), 8772–8776.
Xu, S.H., Nie, Y.Y., Jiang, L.P., Wang, J., Xu, G.Y., Wang, W., Luo, X.L., 2018. Anal. Chem. 90 (6), 4039–4045.
Xue, J., Niu, J., Wu, J., Wu, Z.H., 2014. World J. Clin. Oncol. 5 (4), 730–743.
Yang, C., Dou, B., Shi, K., Chai, Y., Xiang, Y., Yuan, R., 2014a. Anal. Chem. 86 (23), 11913–11918.
Yang, C., Dou, B., Shi, K., Chai, Y., Xiang, Y., Yuan, R., 2014b. Anal. Chem. 86 (23), 11913–11918.
Yang, L., Li, Y., Zhang, Y., Fan, D., Pang, X., Wei, Q., Du, B., 2017a. ACS Appl. Mater. Interfaces 9 (40), 35260–35267.
Yang, L., Zhu, W., Ren, X., Khan, M.S., Zhang, Y., Du, B., Wei, Q., 2017b. Biosens. Bioelectron. 91, 842–848.
Yin, B.C., Liu, Y.Q., Ye, B.C., 2012. J. Am. Chem. Soc. 134 (11), 5064–5067.
Z, L., Y, W., Y, N., S, K., 2015. Biosens. Bioelectron. 70, 246–253.
Zhang, J., Wu, D.Z., Cai, S.X., Chen, M., Xia, Y.K., Wu, F., Chen, J.H., 2016a. Biosens. Bioelectron. 75, 452–457.
Zhang, L., He, Y., Wang, H., Yuan, Y., Yuan, R., Chai, Y., 2015a. Biosens. Bioelectron. 74, 924–930.
Zhang, P., Zhuo, Y., Chang, Y.Y., Yuan, R., Chai, Y.Q., 2015b. Anal. Chem. 87 (20), 10385–10391.
Zhang, S.H., Wen, L., Yang, J.P., Zeng, J.F., Sun, Q., Li, Z., Zhao, D.Y., Dou, S.X., 2016b. Part. Part. Syst. Char. 33 (5), 261–270.
Zhang, X., Bao, N., Luo, X.L., Ding, S.N., 2018. Biosens. Bioelectron. 114, 44–51.
Zhang, X., Ding, S.N., 2017. Sensor. Actuator. B Chem. 240, 1123–1133.
Zhou, X., Xu, W., Wang, Y., Kuang, Q., Shi, Y., Zhong, L., Zhang, Q., 2010. J. Phys. Chem. C 114 (46), 19607–19613.
Zhu, Y., Li, Z., Chen, M., Cooper, H.M., Lu, G.Q., Xu, Z.P., 2012. Chem. Mater. 24 (3), 421–423.
Zhu, Y., Li, Z., Chen, M., Cooper, H.M., Xu, Z.P., 2013. J. Mater. Chem. B 1 (17), 2315–2323.